JVST A
Journal of Vacuum Science & Technology A

Area-selective atomic layer deposition of noble metals: Polymerized fluorocarbon layers as effective growth inhibitors

Cite as: J. Vac. Sci. Technol. A **39**, 022402 (2020); https://doi.org/10.1116/6.0000701
Submitted: 08 October 2020 • Accepted: 05 January 2021 • Published Online: 29 January 2021

Petro Deminskyi, Ali Haider, Hamit Eren, et al.

JVST A
Journal of Vacuum Science & Technology A
ARTICLE
avs.scitation.org/journal/jva

Area-selective atomic layer deposition of noble metals: Polymerized fluorocarbon layers as effective growth inhibitors

Cite as: J. Vac. Sci. Technol. A **39**, 022402 (2021); doi: 10.1116/6.0000701
Submitted: 8 October 2020 · Accepted: 5 January 2021 ·
Published Online: 29 January 2021

View Online Export Citation CrossMark

Petro Deminskyi,[1] Ali Haider,[1] Hamit Eren,[2] Talha M. Khan,[1] and Necmi Biyikli[3,a)]

AFFILIATIONS

[1]UNAM—Institute of Materials Science and Nanotechnology, Bilkent University, Ankara 06800, Turkey
[2]Department of Chemical Engineering, Delft University of Technology, van der Maasweg 9, 2629 HZ Delft, The Netherlands
[3]Department of Electrical and Computer Engineering, University of Connecticut, 371 Fairfield Way, Storrs, Connecticut 06269-4157

Note: This paper is a part of the Special Topic Collection on Area Selective Deposition.
[a)]**Electronic mail:** necmi.biyikli@uconn.edu

ABSTRACT

The increasingly complex nanoscale three-dimensional and multilayered structures utilized in nanoelectronic, catalytic, and energy conversion/storage devices necessitate novel substrate-selective material deposition approaches featuring bottom-up and self-aligned precision processing. Here, we demonstrate the area-selective atomic layer deposition (AS-ALD) of two noble metals, Pt and Pd, by using a plasma-polymerized fluorocarbon layer as growth inhibition surfaces. The contact angle, x-ray photoelectron spectroscopy (XPS), and scanning electron microscopy measurements were performed to investigate the blocking ability of polymerized fluorocarbon (CF_x) layers against ALD-grown metal films. Both Pt and Pd showed significant nucleation delays on fluorocarbon surfaces. Self-aligned film deposition is confirmed using this strategy by growing Pt and Pd on the microscale lithographically patterned CF_x/Si samples. CF_x blocking layer degradation during ozone exposure was analyzed using XPS measurements, which confirmed the oxygen physisorption as the main responsible surface reaction with further hydroxyl group formation on the CF_x surface. Our work reveals that the CF_x layer is compatible with an ozone coreactant until the blocking polymer cannot withstand oxygen physisorption. Our results could potentially be used to investigate and develop radical-assisted AS-ALD processes for a wider selection of materials.

I. INTRODUCTION

Atomic-scale precision manufacturing of next-generation complex three-dimensional (3D) device structures necessitates the development of highly selective bottom-up material deposition strategies. As opposed to the conventional top-down approaches, area-selective deposition (ASD) provides self-aligned processing capability, which enhances the structural precision, while reducing the overall fabrication complexity. The relatively recent efforts in area-selective atomic layer deposition (AS-ALD) unveiled the significant potential of ALD as a bottom-up material synthesis technique, which can be engineered toward achieving surface selectivity.[1–5] Being a surface-chemistry driven vapor-phase synthesis method, ALD features iterative self-limiting growth cycles based on low-temperature ligand-exchange reactions.[6,7] The resulting deposition is highly controllable with submonolayer thickness accuracy, along with excellent 3D conformity and large-area uniformity.[8–14] The main target of AS-ALD efforts is to combine the unique features of ALD with surface selectivity, potentially leading to a versatile self-aligned fabrication toolbox.

Among others, the area-deactivation approach became the main AS-ALD strategy, where self-assembled monolayers (SAMs) or various polymer films are utilized as growth blocking surfaces.[15,16] This way, selective deposition has been reported for oxides[4,17–19] (Al_2O_3, SiO_2, TiO_2, and ZnO) and metals[20–23] (Pt, Pd, Ru, Rh, Ir, and Co). Despite the promising results with various SAM chemistries, this approach suffered mainly from the difficulty in defect-free SAM synthesis, relatively long synthesis time, and CMOS compatibility.[4,24–26] The latest reports by Bent *et al.* show that the time for SAM deposition reduces significantly with vapor-phase

techniques compared with conventional liquid-phase synthesis and yet provides sufficient blocking performance for conventional thermal AS-ALD processes.[1,27] However, both SAM and polymer blocking layers tend to degrade fairly quickly when radical-enhanced coreactants are utilized including plasmas and ozone. This incompatibility with energetic coreactants limits their use to merely thermal-ALD processes, excluding some critical materials.[28,29]

Platinum (Pt) and palladium (Pd) are among the most widely employed noble metals not only for CMOS logic and memory device fabrication[30,31] but also for catalysis,[32] energy conversion,[33] chemical sensing,[34,35] and energy storage.[36] Selective deposition of these noble metals is significantly needed for the fabrication of self-aligned metal-contact placement in 3D nanoscale device structures. Reports on AS-ALD of Pd are mostly related to the controlled synthesis of Pd/Pt core–shell nanoparticles using SAMs as blocking layers.[37] On the other hand, former efforts related to the AS-ALD of Pt include (i) electron-beam induced deposition,[38] which has compatibility issues for large areas and high-aspect-ratio structures, (ii) use of PMMA and polyimide (PI) blocking layers for thermal Pt-ALD that degrade under radical/plasma exposure,[39] and (iii) topographically selective Pt-ALD on the vertical sidewalls of fin structures via ion-implanted ultrathin fluorocarbon films as growth inhibition horizontal surfaces.[2] Selective noble-metal ALD featuring energetic coreactants such as ozone are yet missing. Growth inhibitors needed for such energetic ALD processes should ideally exhibit sufficient radical resistance, a defect/pinhole-free microstructure, CMOS-compatibility, ease of deposition, and thermal stability.[15]

Our previous work on AS-ALD of metal-oxide films where we used inductively coupled plasma (ICP)-polymerized fluorocarbon (CF_x) coatings as blocking layers showed effective ZnO growth inhibition with self-aligned patterning, while no growth blocking efficiency was observed for TiO_2.[40,41] The utilization of a CMOS-standard plasma-polymerized CF_x film along with its relative ease of control revealed this approach with significant potential. In this work, we demonstrate that polymerized fluorocarbon surfaces can function as effective growth inhibitors for ALD-grown Pt and Pd films as well. Besides providing successful growth blocking for Pt and Pd, ozone-assisted Pt-ALD experiments revealed that polymerized CF_x layers are also ozone-compatible. To the best of our knowledge, this is the first demonstration of an AS-ALD process utilizing ozone as a coreactant for noble metals. When compared with the ion-implanted ultrathin CF_x blocking layers,[2] our approach provides a complementary CMOS-compatible solution to inhibit Pt and Pd deposition on nonhorizontal surfaces of 3D nanostructures. This strategy might pave the way for the selective deposition of alternate materials, which necessitate energetic coreactants.

II. EXPERIMENT

A. Film growth

The CF_x layer was deposited on a commercial ICP etch reactor (SPTS MPX-ICP), conventionally used for the deep reactive ion etching (DRIE) process of Si wafers. The deposition of ~60 nm of CF_x was performed for ~70 s using C_4F_8 (99.998% purity, Linde) at a gas flow rate of 70 SCCM under a 400 W radio frequency plasma power at 13.56 MHz. Si (100) reference control samples were solvent-cleaned (acetone, isopropyl alcohol, de-ionized water rinse, and N_2 blow dry) and exposed to O_2 plasma in an asher system (100 W, 50 SCCM) for 2 min before ALD of Pd in order to increase the concentration of hydroxyl groups on the substrate, which should eliminate any possible nucleation delays on the Si surface.[40] The reference control samples for the Pt study were not pretreated in O_2 plasma before the main Pt-ALD growth due to the ozone-based plasma process that increases the hydroxyl groups on the substrate during the deposition experiments. Pt and Pd deposition on bare and CF_x-coated Si (100) samples was accomplished by using trimethyl (methylcyclopentadienyl) platinum(IV) ($MeCpPtMe_3$) and palladium(II) hexafluoroacetylacetonate [$Pd(hfac)_2$] as metal precursors.[42,43] Ozone (O_3) and formalin (CH_2O) were utilized as coreactants for Pt and Pd growth, respectively.[44,45] O_3 was produced from a pure O_2 flow with a Veeco/Cambridge NanoTech Savannah Ozone Generator. ALD experiments with different cycle numbers were carried out at 150 and 200 °C for Pt and Pd, respectively, using a Savannah S100 ALD reactor (Veeco/CambridgeNanoTech Inc.) and N_2 as the carrier and purge gas. The unit ALD growth cycle of Pt consisted of $MeCpPtMe_3$ pulse (0.2 s), N_2 purge (15 s), ozone pulse (0.1 s), and N_2 purge (15 s). The $MeCpPtMe_3$ precursor was preheated to 65 °C and stabilized at this temperature to transport the $MeCpPtMe_3$ vapor to the reaction chamber. On the other hand, the unit ALD cycle of Pd consisted of a $Pd(hfac)_2$ pulse (0.4 s), N_2 purge (10 s), formalin pulse (0.15 s), and N_2 purge (10 s). The $Pd(hfac)_2$ precursor was preheated to 70 °C and stabilized at this temperature prior to the deposition experiments. Formalin was kept at room temperature during the growth. The total stabilization time before growth for both Pt and Pd was ~20 min.

B. Film characterization and patterning

Contact angles of bare and CF_x-coated Si (100) substrates have been measured before and after ALD growth cycles, using the static contact angle measurement setup (OCA 30). A 4 μl-water droplet was dropped on the sample surfaces to measure the contact angle. Film thicknesses of CF_x were determined using a variable angle spectroscopic ellipsometer (V-VASE, J.A. Woollam Co. Inc., Lincoln, NE), which was coupled with a rotating analyzer and xenon light source. Ellipsometric spectra were collected at three angles of incidence (65°, 70°, and 75°) to yield adequate sensitivity over the full spectral range. Film thickness values were extracted by fitting the spectroscopic ellipsometer data using the Cauchy model, while the substrate was set as default Si (100) in V-Vase Woollam software. Elemental composition and chemical bonding states of the metal films were obtained by x-ray photoelectron spectroscopy (XPS) measurements using a Thermo Scientific K-Alpha spectrometer (Thermo Fisher Scientific) with a monochromatized Al Kα x-ray source (a spot size of ~400 μm). All peaks in XPS survey scans are referenced to the C 1s peak for charge correction, and quantification of survey scans has been performed using AVANTAGE software. The surface morphologies of the Pt and Pd-coated samples were determined using a high-resolution FIB-SEM system (FEI, Nova 600i Nanolab), and the cluster size was determined using "IMAGEJ" software. To pattern CF_x via lithography on Si (100) substrates, ~1.4 μm of AZ5214 photoresist (Microchemicals GmbH) was spun on the wafer and was patterned into a checkerboard and parallel striped lines using a suitable photomask and photolithography.

The wafer was then hard baked at 110 °C for 5 min, followed by the ICP polymerization process in the ICP reactor. Once the deposition was complete, the wafer was soaked into acetone for the lift-off process of CF_x layer portions on top of the patterned photoresist. The resulting wafer with a patterned CF_x layer was solvent-cleaned before subsequent metal-ALD growth experiments. An XPS line scan was performed on the resulting Pt and Pd-coated samples to determine the selectivity performance as a function of ALD cycles, using the same XPS system with a spot size of ~100 μm, the scanning step size, and scanning points of 41/43 μm and 100/176 for Pt/Pd, respectively. The structural analysis of the ALD-grown Pt and Pd thin films was performed using grazing-incidence x-ray diffraction (GIXRD) patterns that were recorded in an X'Pert PRO MRD diffractometer (PANalytical B.V., Almelo, The Netherlands) using Cu Kα radiation. Data were obtained within the 2θ range of 30–90° by the summation of ten scans, which were performed using a 0.1° step size and 15 s counting time. Interplanar spacing

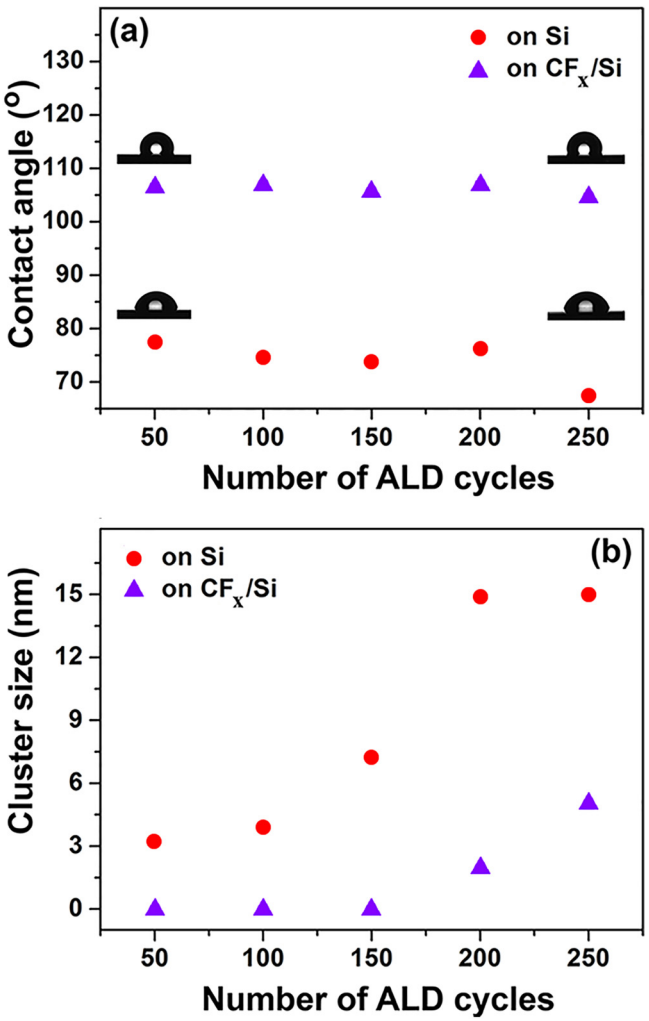

FIG. 1. Variation in (a) contact angle and (b) average Pt cluster size as a function of ALD growth cycles on fluorocarbon coated and bare Si (100) substrates. Exhibiting a relatively constant contact angle, the fluorocarbon surface shows Pt-nucleation inhibition character for more than 150 ALD cycles.

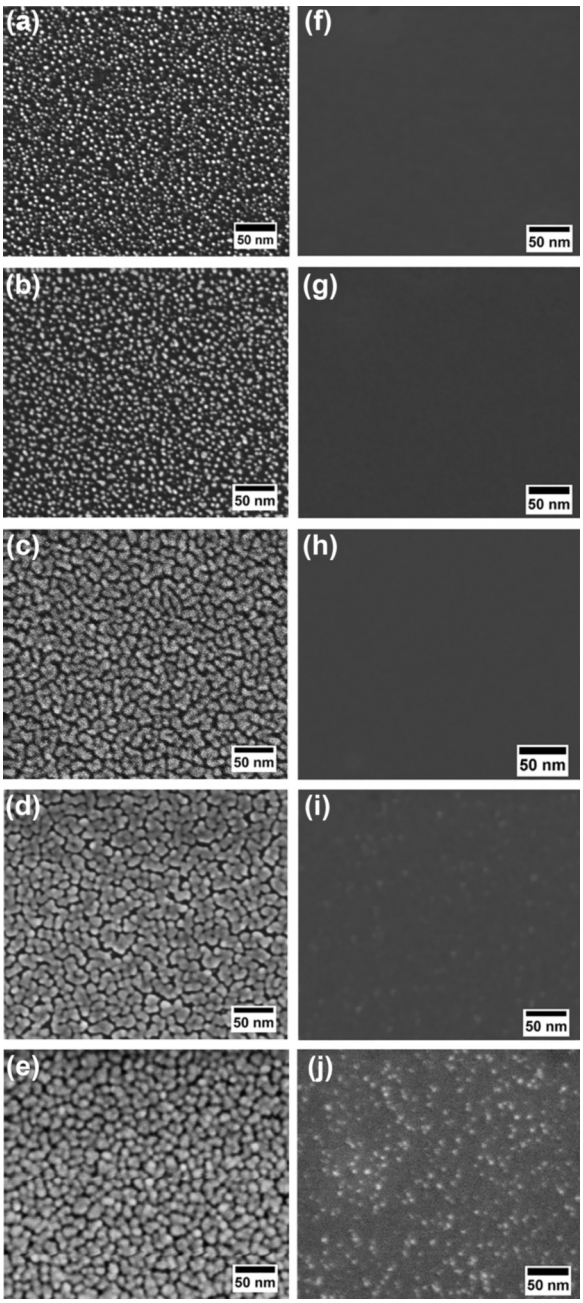

FIG. 2. SEM images of (a)–(e) bare Si (100) and (f)–(j) CF_x/Si (100) sample surfaces at various stages in Pt-ALD growth experiments (a) and (f) 50 cycles; (b) and (g) 100 cycles; (c) and (h) 150 cycles; (d) and (i) 200 cycles; and (e) and (j) 250 cycles.

TABLE I. Variation in Pt and O at. % on CF_x/Si samples and the selectivity value as a function of ALD cycles.

Number of ALD cycles	CF_x/Si Pt at. %	CF_x/Si O at. %	Pt/Si to Pt/CF_x selectivity
50	—	1.03	~1
100	0.01	1.57	
150	0.01	1.81	
200	0.1	2.17	~0.99
250	2.62	4.4	~0.95

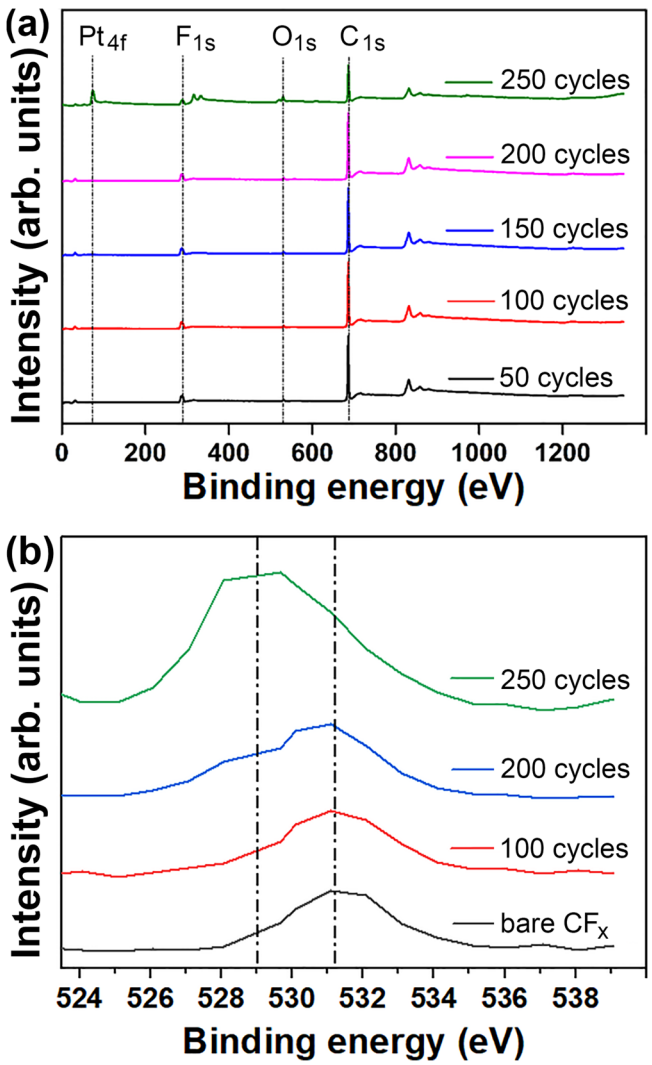

FIG. 3. (a) XPS survey scans of the CF_x/Si (100) sample after 50, 100, 150, 200, and 250 Pt-ALD cycles, depicting a 200-cycle nucleation delay on the polymerized CF_x surface; (b) HR-XPS scans of O 1s obtained on CF_x/Si (100) after 0, 100, 200, and 250 Pt-ALD cycles.

(d_{hkl}) values were calculated from peak positions using Bragg's law. The lattice parameter was calculated by using the experimentally extracted d_{hkl} values in Eq. (1), which relates the interplanar spacing (d_{hkl}), miller indices (hkl), and the lattice parameter (a_0) to a face-centered cubic (fcc) crystal system,

$$d_{hkl} = \frac{a_0}{\sqrt{h^2 + k^2 + l^2}}. \tag{1}$$

To determine the growth selectivity values for Pt and Pd as a function of ALD cycles, we used Eq. (2), which is based on the measured XPS elemental concentrations of Pt or Pd on CF_x (nongrowth) and Si (growth) surfaces,

$$\text{Selectivity} = \frac{A_{\text{Si}} - B_{\text{CFx}}}{A_{\text{Si}}}, \tag{2}$$

where A_{Si} and B_{CFx} are the atomic percent of the ALD deposited material on Si and CF_x surfaces, respectively. The sensitivity of our selectivity numbers is, therefore, limited by the XPS detection limit, which is typically around or slightly higher than 0.01 at. %.

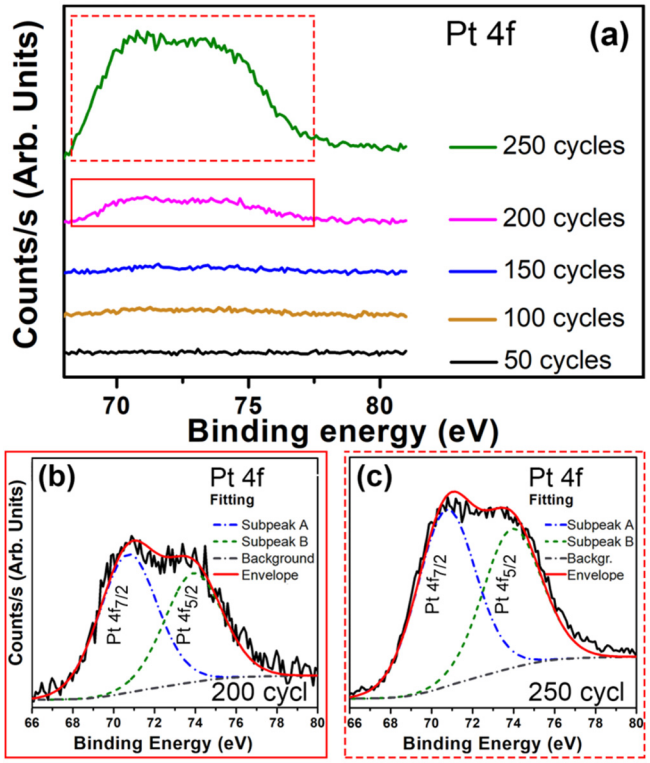

FIG. 4. HR-XPS survey scans of Pt 4f obtained on (a) CF_x/Si (100) after 50, 100, 150, 200, and 250 Pt-ALD cycles; (b) HR-XPS Pt 4f peak fitting for the 200-cycle CF_x/Si (100) sample; and (c) Pt 4f peak fitting for 250-cycle CF_x/Si (100) sample.

III. RESULTS AND DISCUSSION

A. Pt nucleation and selectivity

1. Pt nucleation: CF_x versus Si (100) surfaces

In the first part of our selective deposition study, Pt film nucleation and growth behavior on CF_x and Si surfaces via ozone-based low-temperature ALD are explored. Initial contact angles of Si and CF_x/Si samples before the ALD cycles were measured as ~71° and ~114°, respectively. After the initial 50 ALD cycles, the contact angles on the same samples were measured as 77.4° and 106.4°, respectively, marking an increase for Si and a decrease for CF_x surfaces. The contact angle on Si (100) decreased to ~67.4° after 250 Pt-ALD cycles, while it remained almost unchanged for the CF_x-coated sample with a relatively narrow fluctuation between ~104° and 106°

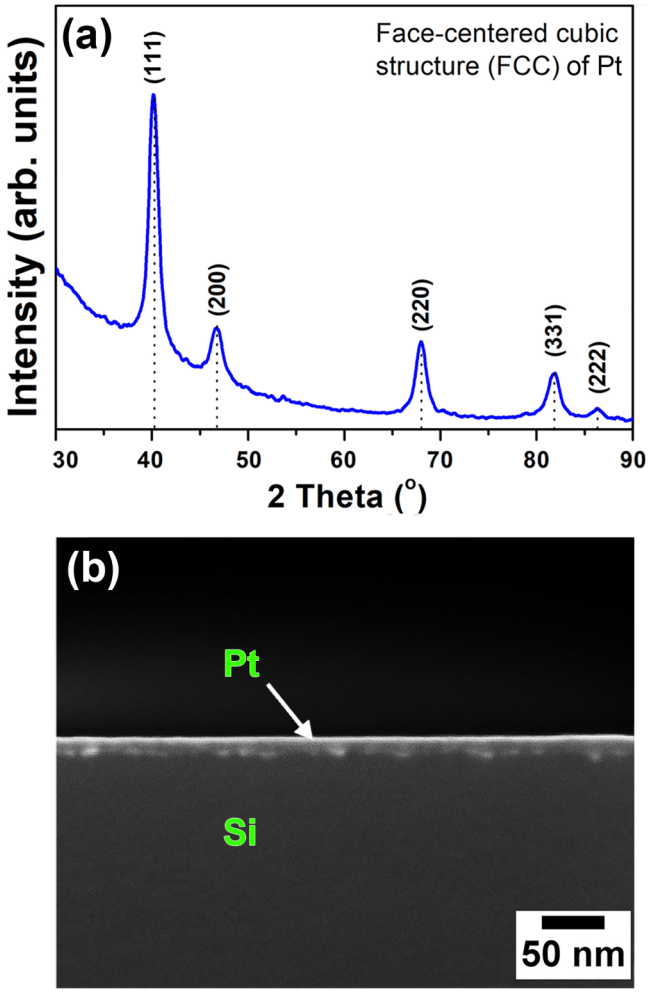

FIG. 5. (a) GIXRD pattern of the Pt film deposited on the Si(100) substrate at 150 °C. (b) Cross-sectional SEM image of the Pt/Si sample showing the total thickness (~20 nm) of the Pt film.

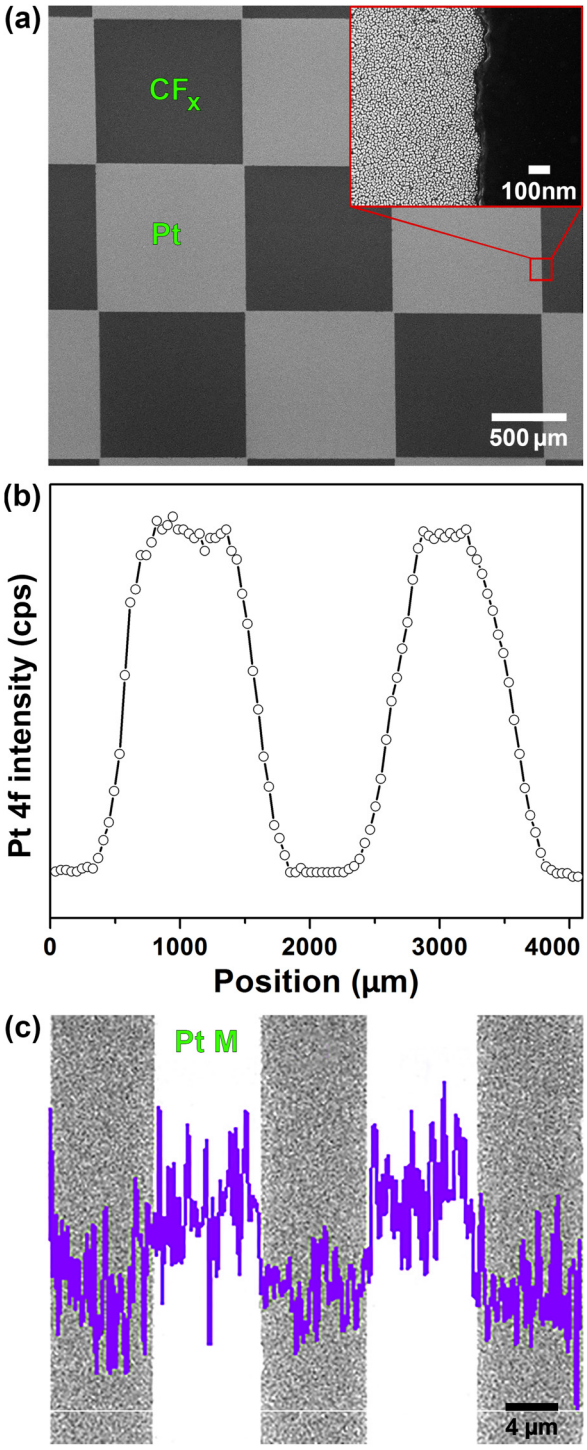

FIG. 6. (a) SEM image and (b) XPS Pt 4f line scan obtained from Pt-ALD grown on the mm-scale patterned CF_x/Si (100) sample. (c) EDX Pt M line scan superposed on the SEM image obtained from the µm-scale CF_x/Si (100) patterned sample after 180 Pt-ALD cycles.

up to 250 cycles [Fig. 1(a)]. Subsequently, we analyzed the evolution of Pt nucleation by measuring the Pt-island/cluster size on Si and CF_x samples as a function of ALD cycles. Figure 1(b) shows how the average Pt cluster size evolved on both sample surfaces with increasing the number of ALD cycles, which clearly indicates a considerable nucleation delay on the CF_x surface. While no Pt clusters were detected up to 150 cycles, ~2 and ~5 nm Pt clusters were observed on CF_x samples after 200 and 250 ALD cycles, respectively, with relatively low density and surface coverage with respect to the Si (100) reference samples. On the other hand, Pt nucleated easily on the Si (100) surface exhibiting high-density ~3 nm sized Pt clusters after the initial 50 ALD cycles, which increased and saturated up to ~15 nm for 200 and higher ALD cycles.

Figures 2(a)–2(j) show the obtained images from the Si (100) and CF_x sample surfaces after 50, 100, 150, 200, and 250 ALD cycles, respectively. The initial 50 cycle results clearly reveal successful Pt nucleation on Si (100) with an increase in both the Pt nanoparticle (NP) density and cluster size, leading toward coalescence into larger islands (~15 nm for 200+ cycles) and an eventually complete surface coverage resulting in a continuous Pt film. However, in contrast to the bare Si (100) sample, the CF_x/Si sample surface is free from any HR-SEM-detectable Pt nucleation at the end of 150 ALD cycles. Pt nucleation on CF_x becomes evident only after 200 ALD cycles with an initial average Pt-cluster diameter of ~2 nm and a relatively nonuniform surface distribution. As a result, the initial Pt NP seeds on the CF_x surface function as growth centers during further ALD cycles featuring half-cycle exposures of $C_9H_{16}Pt$ and ozone. The average Pt cluster size further increases to ~5 nm at 250 ALD cycles, confirming the loss of Pt growth inhibition character of CF_x surface beyond 200 cycles.

Table I summarizes how the platinum and oxygen content from the surface of the CF_x/Si and Si (100) samples evolves during ALD cycles via XPS survey scans. Other than the Pt and O content—more detailed information related to the elemental composition of Si, C, and F is presented in Tables SI and SII in the supplementary material.[56] XPS measurements of the CF_x sample surface show the absence of a detectable Pt signal for 50 and 100 ALD cycles. After 150 ALD cycles, a very weak Pt signal is detected, corresponding to only ~0.01 at. %, which increases by almost an order of magnitude—but still relatively low (~0.07 at. %) for 200 ALD cycles. A further increase in Pt-ALD cycles up to 250 cycles indicates a stronger increase in the Pt content to ~2.6 at. %, confirming the practical Pt nucleation onset for ALD cycles around 200.

The combination of the adsorption of the noble metal precursor and the use of reactive ozone starts to show its effect on the ICP-polymerized CF_x surface only after 200 ALD growth cycles. XPS measurements of the CF_x-coated sample exposed to 250 Pt-ALD cycles show the oxygen content fluctuating within ~2–4 at. %. It confirms the relative stability of the ICP-polymerized CF_x surface against degradation during reactive ozone exposure until the formation of hydroxyl groups (that behave like nucleation centers for Pt growth) and the subsequently adsorbed Pt on the surface. To the best of our knowledge, this result represents the first demonstration of a selective ALD process featuring a reactive ozone coreactant for Pt deposition.

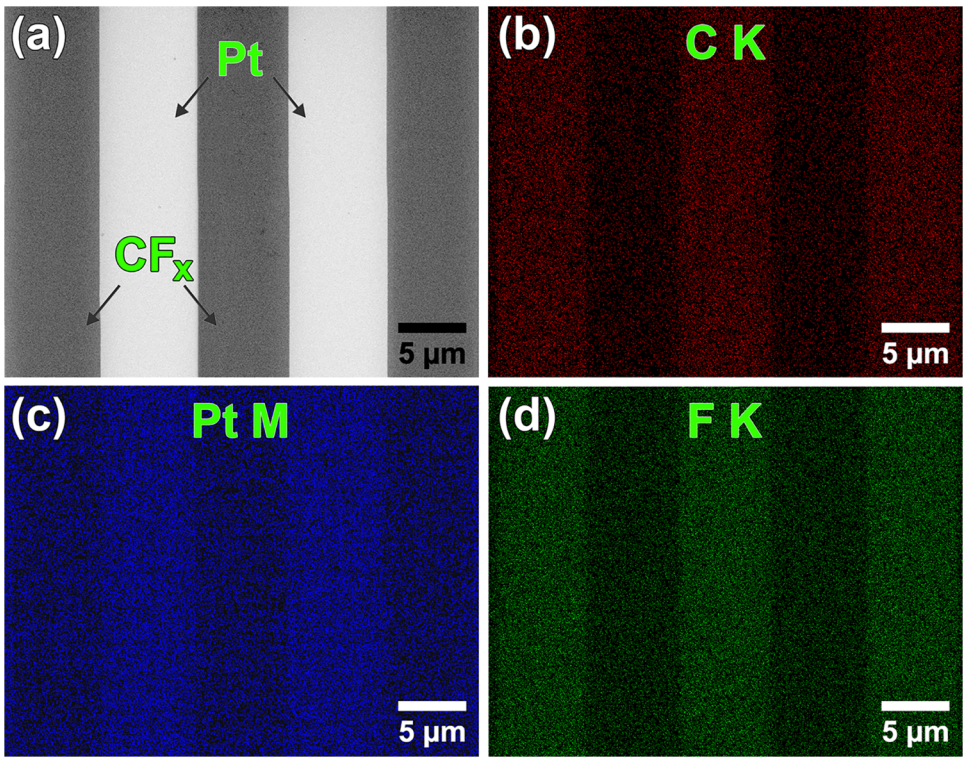

FIG. 7. SEM image of (a) Pt/CF_x self-aligned patterned sample after the 180-cycle Pt-ALD experiment. Elemental mapping of (b) C K, (c) Pt M, and (d) F K signals.

Figure 3(a) shows the XPS survey scan results obtained for CF_x/Si samples recorded at 50, 100, 150, 200, and 250 ALD cycles. While detecting C 1s, O 1s, and F 1s peaks from the CF_x surface, the absence of the Pt 4f peak confirms the successful Pt nucleation inhibition for more than 150 ALD cycles. These results confirm the effective nucleation inhibition behavior of ICP-polymerized CF_x films as growth blocking surfaces for Pt deposition. Moreover, the XPS survey scan results provide excellent correlation with SEM observations as well as contact angle measurements and cumulatively approve that CF_x inhibits the Pt nucleation process for ~200 growth cycles, which is equivalent to a growth blocking thickness of ~17 nm. The ~0.99 selectivity at 200 cycles drops to ~0.95 at 250 ALD cycles.

Figure 3(b) shows the analysis study on the reaction resistance of the fluorocarbon layer exposed to ozone-based growth reactions via investigating the O 1s peaks on the CF_x/Si substrate before and after 100, 200, and 250 cycles of Pt-ALD growth cycles from the measured XPS scans. O 1s is detected on the CF_x substrate before and after Pt growth, with the O 1s peak located at 531.1 eV (I) corresponds to hydroxyl groups (OH) on the surface of CF_x that is in good agreement with the hydroxide signal (531.5 ± 0.5 eV), which is a typical value for binding energies for oxides.[46] We also note

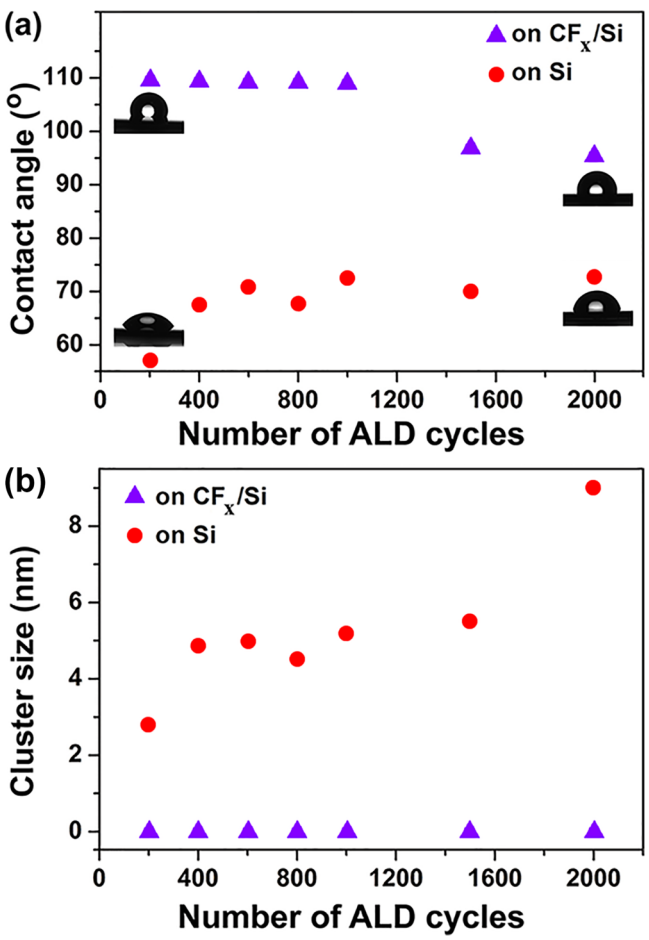

FIG. 8. Variation in (a) contact angle; (b) average Pd-cluster size with number of ALD cycles on CF_x/Si and bare Si (100) samples.

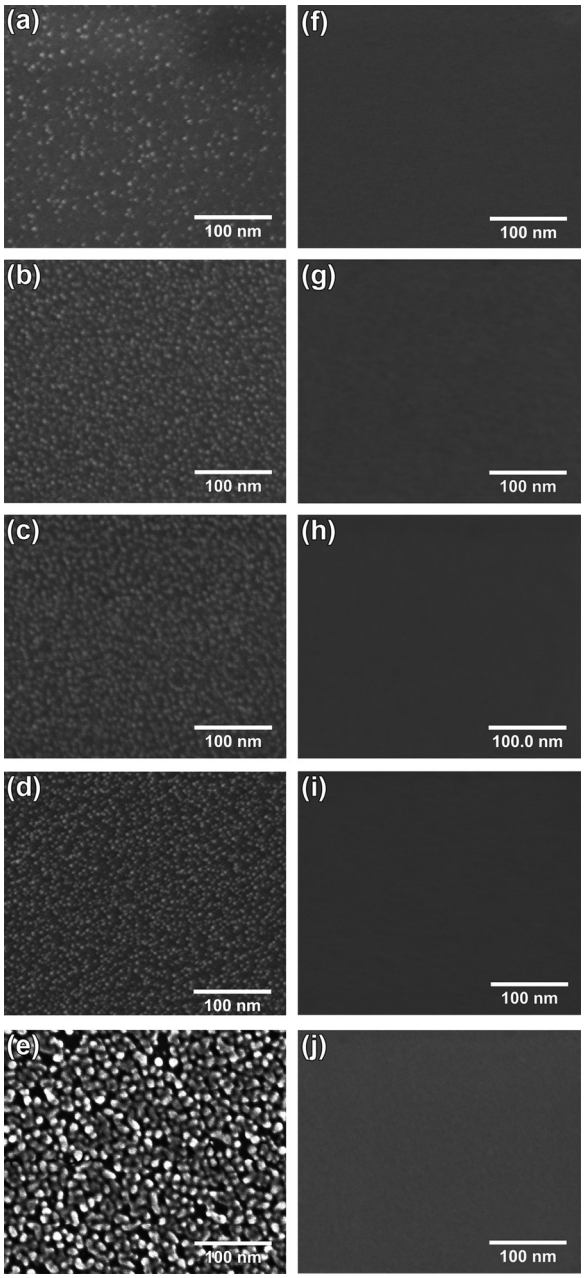

FIG. 9. HR-SEM images of the substrate surfaces of (a)–(e) bare Si (100) samples and (f)–(j) CF_x/Si (100) samples at various stages of the Pd-ALD experiment: (a) and (f) 200 cycles, (b) and (g) 600 cycles, (c) and (h) 1000 cycles, (d) and (i) 1500 cycles, and (e) and (j) 2000 cycles.

another interesting observation: on the CF_x surface, the O 1s peak is broadening to lower binding energies with the peak intensity at 529.7 eV (II) for 250 cycles of Pt-ALD, which could be assigned to the oxygen atoms directly bound to metallic Pt.[47,48] The mechanism of the Pt nucleation on CF_x is currently not fully understood. We hypothesize that during the ozone half-reaction, oxygen is slowly physisorbed onto the CF_x film surface. This diffusion is likely enhanced during additional ozone exposure cycles. In the meantime, during the $MeCpPtMe_3$ half-reaction, hydroxyl groups form on the centers of oxygen vacancies that create favorable nucleation centers for further Pt growth initiation. Although the hydroxyl groups are created on the CF_x surface, the amount of Pt that could be chemisorbed on such active sites is still under the XPS detection limit up to 150 ALD cycles.

Figure 4 shows Pt 4f HR-XPS scans measured on CF_x/Si samples and HR-XPS scans taken after 50, 100, 150, 200, and 250 cycles of Pt-ALD. XPS measurements of CF_x-coated Si samples after 50, 100, 150, 200, and 250 cycles of Pt-ALD show no considerable Pt signal up to 200 cycles [Fig. 4(a) and Table SIII in the supplementary material].[56] At 200 and 250 cycles, we started to observe signals in the range of 67–79 eV corresponding to Pt 4f peaks. After XPS data fitting, we deconvoluted the Pt 4f peak into two well-separated ($\Delta = \sim 3.3$ eV) spin--orbit components with a height ratio of 1:0.77 [Figs. 4(b) and 4(c)]. For the 200-cycle sample, Pt 4f peaks centered at 70.7 ± 0.2 eV (subpeak A—Pt $4f_{7/2}$) and 74.0 ± 0.2 eV (subpeak B—Pt $4f_{5/2}$) are assigned to the metallic Pt(0) bonding. Likewise, we deconvoluted the Pt 4f peak for the 250-cycle sample into two individual peaks centered at 70.7 ± 0.2 eV (subpeak A—Pt $4f_{7/2}$) and 74.0 ± 0.2 eV (subpeak B—Pt $4f_{5/2}$), which are assigned to the same metallic Pt. Pt $4f_{7/2}$ and Pt $4f_{5/2}$ are not clearly separated from each other, which could be attributed to the platinum oxidation that resulted in the shoulder formation.[49] Furthermore, the slightly lower binding energies (70.7 ± 0.2 eV) possibly indicate the presence of smaller Pt particles, which are also in good agreement with the cluster size dependence on the total ALD cycle number [Figs. 1(b) and 2(d)–2(j)].[50] Additional information related to the Pt HR-XPS scans measured on Si samples is represented in the supplementary material,[56] which is in good agreement with the observed trend on CF_x/Si (100) samples: oxide states within the initial 50–100 cycles were transformed to metallic states at higher ALD cycle numbers. The HR-XPS scans of Pt 4f on Si (100) are provided in Fig. S1 in the supplementary material.[56]

Another important observation was the thickness stability (~60 nm) of CF_x blocking layer, regardless of the Pt-ALD cycles that featured reactive ozone exposures. The absence of any decrease in CF_x thickness under ozone cycles might be attributed to the

TABLE II. Variation in Pd at. % on CF_x/Si samples and the calculated selectivity value as a function of ALD cycles.

Number of ALD cycles	CF_x/Si Pd at. %	Pd/Si to Pd/CF_x selectivity
200	0.02	~1
400	0.03	
600	0.03	
800	0.03	
1000	0.02	
1500	0.03	
2000	0.12	~0.99

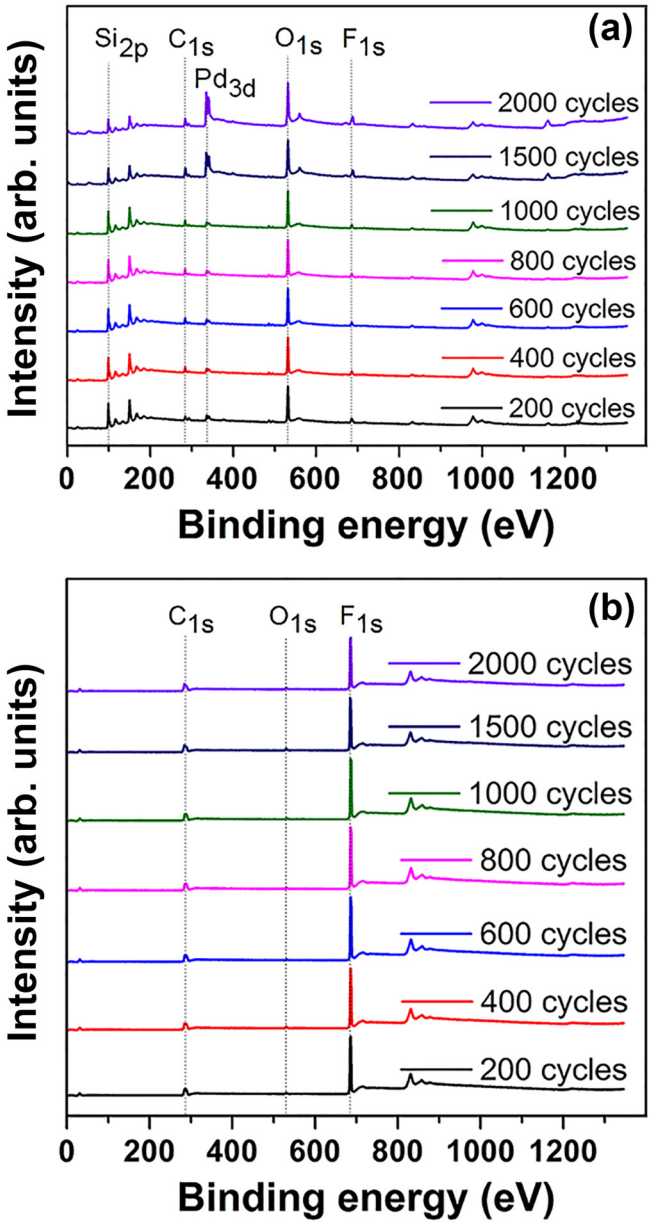

FIG. 10. XPS survey scans of (a) Si (100) and (b) CF_x/Si samples at various stages of Pd-ALD growth experiments, which confirm effective Pd-nucleation blocking of the CF_x surface up to 2000 Pd-ALD cycles.

relatively strong C–F bonding that prevented any film etching reaction during excessively long ozone exposure at temperatures up to 150 °C. In addition to the inherent unreactive nature of CF_x, stability in the thickness of the CF_x layers indicates the potential for a further investigation of AS-ALD under alternate energetic coreactants and plasma chemistries in radical-assisted ALD processes.

The structural properties of the Pt film were studied by GIXRD. Figures 5(a) and 5(b) depict the XRD pattern and SEM image of the as-prepared Pt film with ~20 nm thickness. The measured pattern was indexed by a fcc crystal system (ICDD reference code: 00-004-0802). The (111), (200), (220), (311), and (222) peak reflections were observed at the 2θ values of 40.2°, 46.6°, 67.9°, 81.9°, and 86.3°, respectively. The XRD peaks of the Pt thin film were comparable to those of the corresponding bulk Pt material.[49] The lattice parameter *a* was calculated using 2θ positions of the (111) reflection. Interplanar spacing (d_{hkl}) values were calculated from Bragg's law and the *a*-axis lattice parameter was calculated as ~3.88 Å, which matches well with the bulk value for Pt (3.92 Å).

2. Selective Pt deposition and self-aligned patterning

Self-aligned patterning of Pt films is demonstrated using selective Pt deposition on lithographically patterned CF_x/Si samples with 180 Pt-ALD cycles and by EDX analysis, XPS line scan

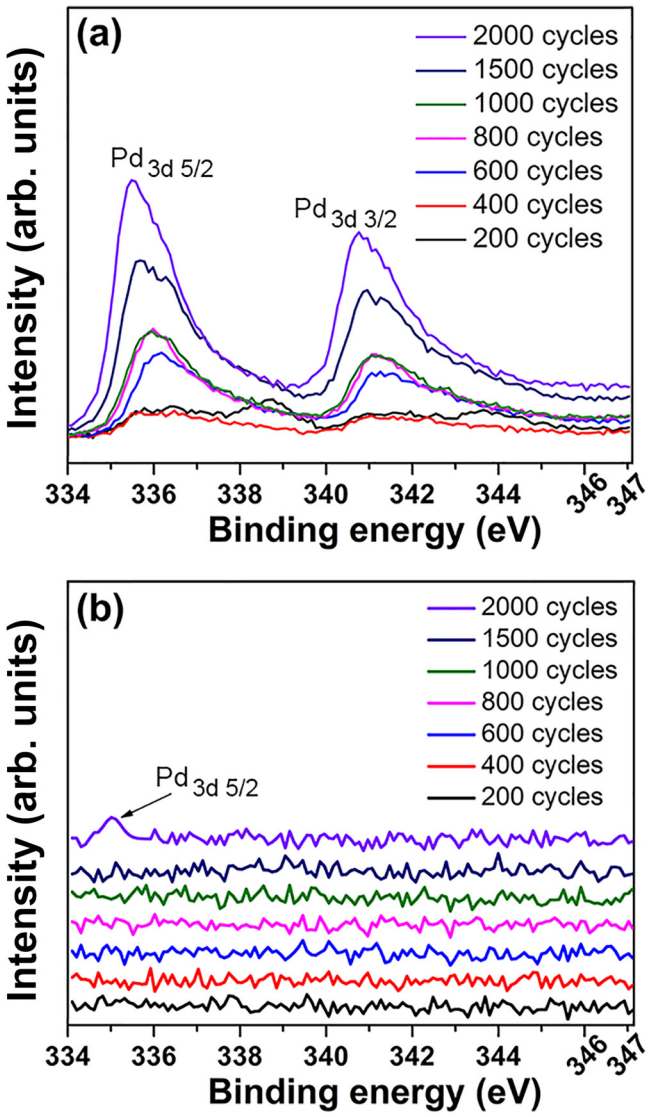

FIG. 11. HR-XPS survey scans of Pd 3d obtained at different stages of Pd-ALD on (a) Si (100) and (b) CF_x/Si (100), confirming the near-ideal complete blocking of Pd deposition on the CF_x surface.

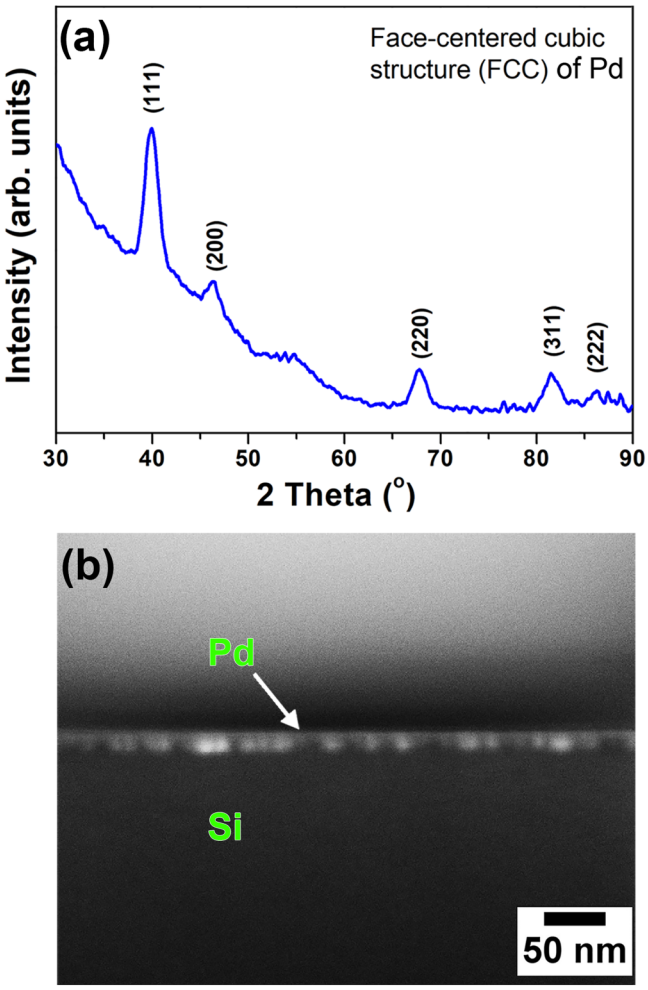

FIG. 12. (a) GIXRD pattern of Pd film selectively deposited on the Si (100) substrate at 200 °C. (b) Cross-sectional HR-SEM image of the Pd/Si sample with the ~15 nm thick Pd film.

measurements, and HR-SEM imaging, as shown in Figs. 6(a)–6(c). An XPS line scan was performed on mm-scale Pt patterns [Fig. 6(a)] where Pt 4f intensity was measured [Fig. 6(b)]. The Pt 4f peak is observed only in bright-looking regions where the CF_x layer was lifted off with the Si (100) growth surface exposed, while CF_x regions with a dark color contrast exhibit Pt 4f intensity as a background (noise-floor) signal, confirming the absence of Pt deposition on the CF_x nongrowth surface. The reason for a gradual increase in Pt 4f intensity at the CF_x/Si (100) boundaries can be attributed to the relatively larger spot size of the monochromatized Al Kα x-ray source that was set to ∼100 μm during the XPS line scan, as well as the value of scanning steps and a number of scanning points utilized. At the CF_x/Pt interface, due to the relatively large XPS spot size, we simultaneously detect signals from both CF_x and Pt covered surfaces, which cause a gradual increase in the observed Pt intensity. The uniform blocking of Pt growth on the CF_x pattern was confirmed by the HR-SEM image, which depicts a sharp CF_x/Pt interface [see Fig. 6(a)]. Figure 6(c) shows the EDX line scan measurement, revealing Pt M x-ray quanta being detected along the scan line. As expected, the intensity of Pt M x-ray quanta increases only in line patterns where CF_x was lifted off with the exposed Si (100) surface, which reaffirms the effective self-aligned patterning of Pt line structures at the micro scale.

EDX elemental mapping images are shown in Fig. 7; this mapping is performed to indicate the coverage and distribution of Pt, C, and F elements on the patterned CF_x/Si sample surface. Figure 7(a) shows the SEM image of patterned Pt line features through which elemental maps of Pt, C, and F are collected. Figures 7(b)–7(d) show the elemental maps of C K, Pt M, and F K, respectively. These results confirm both successful self-aligned patterning of CF_x and area-deactivated AS-ALD deposition of Pt up to at least 180 ALD cycles. We have used 180 cycles of Pt-ALD to avoid any Pt nucleation that appeared after 200 growth cycles and to demonstrate optimal conditions for Pt nucleation on the Si growth surface, while the CF_x nongrowth surface shows near-ideal nucleation blocking.

B. Pd nucleation and selectivity

1. Pd nucleation: CF_x versus Si (100) surfaces

The Pd-ALD growth experiments using $Pd(hfac)_2$ and formaline precursors were carried out on CF_x-coated and bare Si (100) substrates for 200, 400, 600, 800, 1000, 1500, and 2000 ALD cycles. Figures 8(a) and 8(b) depict the variation in the measured contact angle and average Pd-cluster size of the exposed substrates as a function of the number of ALD cycles. At the end of the first 200 Pd-ALD cycles, the contact angle of the Si sample decreased from ∼71° to ∼57°, while the CF_x-coated sample exhibited only a slight decrease from ∼114° to ∼110°. With a further increase in ALD cycles up to 2000 cycles on Si (100) samples, the contact angle exhibited an increase and fluctuated between ∼68° and 72°. The increase of the contact angle with increasing the number of ALD cycles [Fig. 8(a)] can be attributed to the topography [the impact of the surface roughness due to the changes in palladium nanoparticle dimensions (Fig. 8(b)].[50,51] In contrast, CF_x samples exhibited a rather stable contact angle value of ∼109°, almost independent from the number of ALD cycles up to 1000 cycles. However, the contact angle decreased to ∼95° for Pd growth cycles higher than 1500, signaling a possible nucleation onset for Pd film growth on the CF_x surface. These results indicate that the plasma-polymerized CF_x layer retains its rather hydrophobic and inert character up to more than 1000 Pd-ALD cycles, while its surface state starts to show an initial change toward 1500 ALD cycles.

Subsequently, SEM measurements were performed to visualize the nucleation behavior of Pd on CF_x-coated and bare Si (100) sample surfaces. Figures 9(a)–9(j) represent HR-SEM images of Pd-ALD on bare and CF_x-coated Si (100) samples after 200, 600, 1000, 1500, and 2000 ALD cycles, respectively. In agreement with the contact angle measurements, HR-SEM images apparently show no measurable evidence of Pd growth on the CF_x surface up to the maximum 2000 ALD cycles that we have studied. This is in strong contrast to Pd nucleation and growth behavior on Si (100), where Pd nucleates right away and Pd-NPs are apparent after the first 200

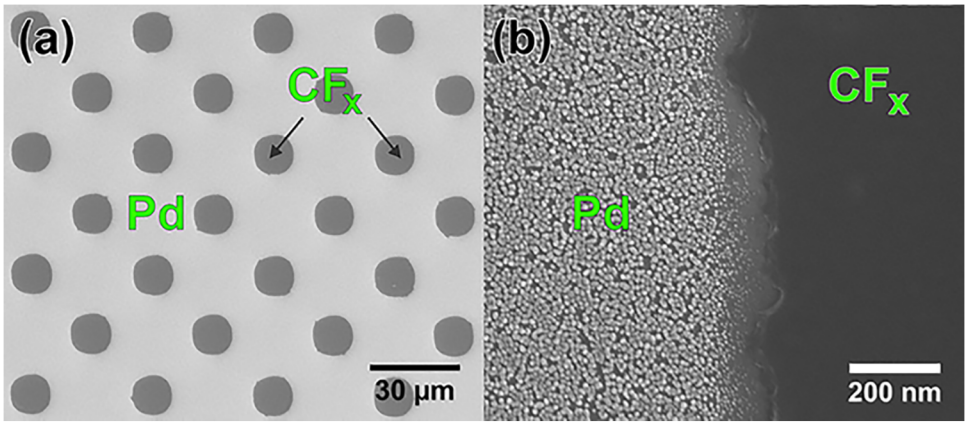

FIG. 13. SEM and HR-SEM images of the patterned CF_x/Si sample surface after 2000 cycles of Pd-ALD. (a) SEM image showing the contrast of Pd-coated Si (100) and uncoated CF_x regions. (b) HR-SEM image of the Pd/CF_x interface, which demonstrates the absence of Pd nucleation on the ICP-polymerized CF_x blocking layer.

ALD cycles. A further increase in Pd growth cycles on Si (100) leads to an increase in the density and size of Pd-NPs, eventually coalescing into larger and densely packed Pd islands, with an estimated effective film thickness of ~10 nm. On the other hand, the polymerized CF_x film retained its growth blocking character until the testing of the maximum number (2000) of growth cycles. Literature reports indicate that organic blocking layers used for selective ALD exhibit degradation beyond a certain number of ALD growth cycles, eventually resulting in unwanted nucleation and failure to block film growth. This result has, in part, been attributed to cumulatively long exposures of the organic blocking layers to relatively high substrate temperatures. Although the CF_x layer showed significant inhibition against Pd growth up to 2000 ALD cycles (12 h exposure at 200 °C), it does not imply that CF_x will not fail eventually. These results are achieved without a detailed and systematic recipe optimization for Pd growth since the main aim of this study was to explore the noble metal nucleation inhibition properties of the polymerized CF_x layers. As a follow-up study, the ALD growth conditions might be further adjusted to achieve enhanced selectivity performance via shorter unit ALD cycles.

Table II summarizes the quantification of the Pd content (at. %) from XPS survey scans for Pd on CF_x/Si and bare Si (100) substrates. Other than the Pd content, information related to the elemental composition of Si, C, O, and F is presented in Table SIV in the supplementary material.[56] The amount of Pd on the CF_x/Si samples was calculated as ~0.02% using XPS data, regardless of the number of ALD cycles up to 1500 cycles. This result again confirms that CF_x is efficiently blocking Pd nucleation for at least 1500 ALD cycles. With an additional 500 cycles, the 2000-cycle Pd-ALD sample on the CF_x/Si substrate indicates a slight but yet observable increase to ~0.12%. Despite the fact that this atomic percentage corresponds to typically less than a monolayer of Pd deposition, we can safely claim that the complete Pd-nucleation blocking property of ICP-polymerized CF_x is degraded after 2000 cycles of Pd-ALD. The Pd content on bare Si (100) substrate samples, on the other hand, shows a strongly correlated increase with a number of ALD growth cycles, confirming the absence of Pd nucleation inhibition of Si surfaces.

XPS survey scan data from both Si and CF_x samples were recorded at various growth stages to determine the surface elemental composition as well as the chemical bonding states (see Fig. 10). C 1s, O 1s, and F 1s peaks were detected from the CF_x surface, irrespective of the number of Pd-ALD cycles. The absence of the as detectable Pd 3d peak corroborates the previous findings that CF_x successfully blocks Pd film growth throughout the 2000 ALD cycles [Fig. 10(b)]. On the other hand, on the bare Si (100) surface, the presence of relatively strong Pd 3d peak signals right after the very first 200 ALD cycles confirms the Si (100) surface as an efficient growth surface with no or small nucleation delay [Fig. 10(a)].

To further analyze and confirm Pd nucleation inhibition on the CF_x surface, Pd 3d high-resolution XPS (HR-XPS) scans were carried out, and the resulting peak spectra measured on Si (100) and CF_x/Si (100) as a function of total ALD cycles are shown in Fig. 11. All recorded peaks were fitted after a charge correction with respect to the adventitious C 1s spectra component (C–C, C–H), with the binding energy set to 284.8 eV. HR-XPS spectra exhibit Pd 3d5/2 and Pd 3d3/2 spin–orbit doublet peaks for the ALD-grown Pd

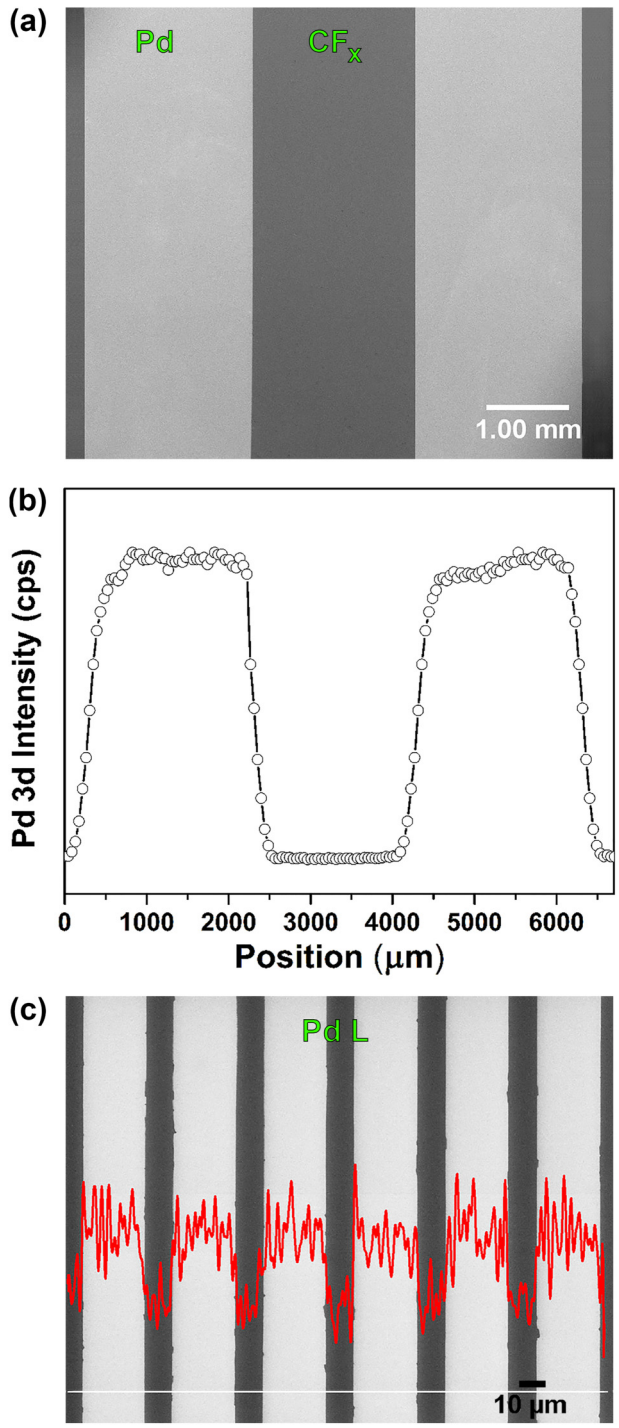

FIG. 14. (a) and (b) SEM image and XPS Pd 3d line scan measurements obtained from 2000 cycle Pd-ALD samples grown on mm-scale patterned CF_x/Si (100) features, respectively. (c) EDX Pd L line scan superposed on the SEM image obtained from the μm-scale CF_x/Si (100) patterned sample after 2000 Pd-ALD cycles.

on bare Si (100) substrates, which represent the growth surface for our experiments. The detected bonding species, their corresponding spectral lines, and binding energy values for the grown Pd film have been summarized in Table SV in the supplementary material.[56] For the initial 200 and 400 growth cycles, Pd–O and Pd–O_x bonding schemes have also been detected in addition to the main Pd–Pd core level bonding. Figure 11(a) shows that beyond 400 growth cycles, Pd 3d5/2 and Pd 3d3/2 peaks corresponding only to Pd–Pd bonding interactions have been detected, confirming the formation of small Pd clusters leading to larger Pd agglomerations and eventually Pd thin films with complete surface coverage.[52,53] On the contrary, no detectable Pd signal is observed in the HR-XPS data obtained from the CF_x/Si samples [Fig. 11(b)] from which it can be inferred that there is near-ideal Pd nucleation inhibition on the CF_x blocking layers up to 2000 ALD cycles.

Figure 12 displays the XRD pattern and SEM image of the as-prepared ∼15 nm thin film, showing the characteristic of the property of crystalline Pd. The exhibited pattern was indexed by the fcc crystal system (ICDD reference code: 00-046-1043). The (111), (200), (220), (311), and (222) peak reflections were observed at the 2θ values of 39.9°, 46.4°, 67.7°, 81.4°, and 86.2°, which are in agreement with previously reported results.[54] The lattice parameter *a* was similarly calculated using 2θ positions of (111) reflection. The extracted *a*-axis lattice parameter was 3.91 Å, which matches well with the bulk lattice parameter value for Pd (3.89 Å).[55]

2. Selective Pd deposition and self-aligned patterning

Similar to our selective Pt deposition study, we carried out self-aligned Pd film patterning experiments via selective Pd deposition on lithographically patterned CF_x/Si substrates. Positive CF_x patterns were formed for the analysis and visualization of possible edge effects in selective Pd growth on Si (100) and growth inhibition on CF_x, respectively. Pd deposition was carried out for 2000 ALD cycles on patterned CF_x/Si samples, which are subsequently characterized by HR-SEM, EDX line-scan, EDX elemental mapping, and XPS line scan measurements. Figures 13(a) and 13(b) show SEM images of the Pd patterns, which legibly indicate the selective deposition of the Pd metal (brighter regions) along with a clear and uncoated CF_x surface (darker circular spots). The HR-SEM image from the Pd/CF_x interface shows no Pd deposition signs on top of the polymerized CF_x patterns, except a narrow transition region (50–100 nm) corresponding to the width of the lifted-off CF_x layer sidewall. Within these transition areas, Pd nanoparticles

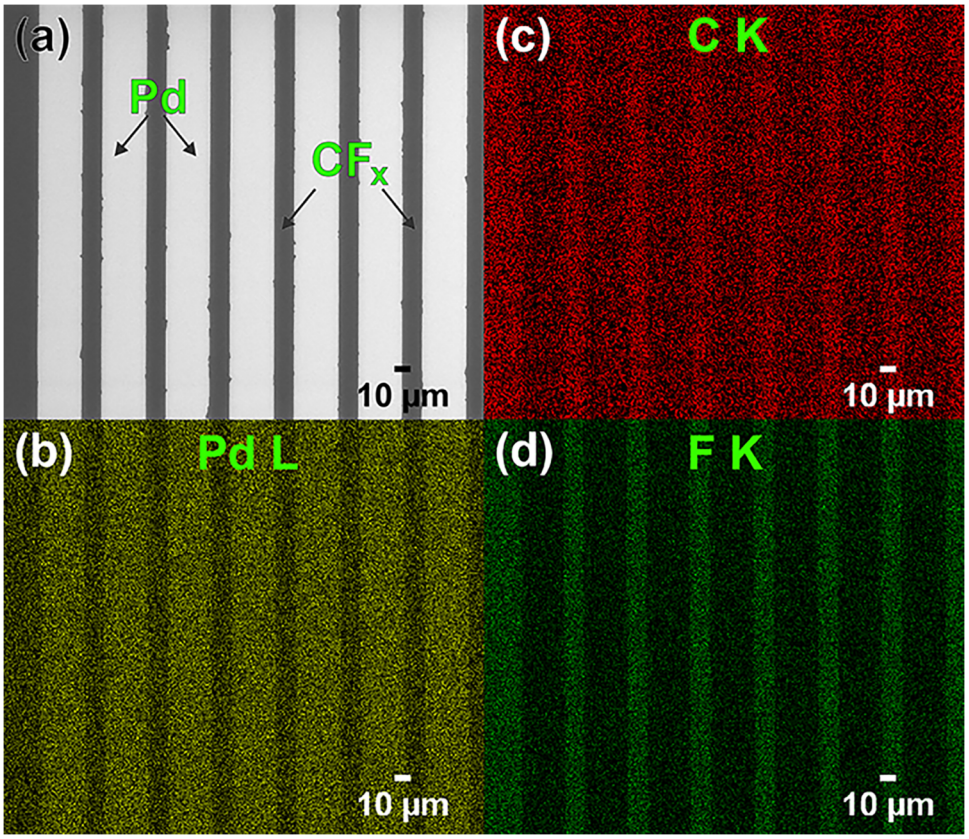

FIG. 15. SEM image of (a) Pd/CF_x patterned sample after 2000-cycle Pd-ALD experiment. Elemental mapping of (b) Pd L, (c) C K, and (d) F K signals.

with smaller cluster size and lower density are observed most probably due to the imperfections of the conventional photolithographic patterning process.

To analyze the elemental composition variation along the Pd/CF_x patterns, EDX and XPS line scans were performed, as depicted in Fig. 14. The XPS line scan was performed on larger mm-scale Pd patterns [Fig. 14(a)] as the survey spectra for this measurement were recorded with an x-ray beam size of 400 μm, along with ~50 μm steps between each data point. Pd 3d intensity was measured in terms of counts per second versus spatial location along the line [Fig. 14(b)]. A considerable contrast is observed between the Pd 3d peak signal intensity obtained from the lifted-off Si (100) regions where Pd has grown without a significant nucleation delay and CF_x patterns which blocked Pd nucleation effectively, confirming a signal intensity equal to the noise floor of the XPS system. The EDX line scan [Fig. 14(c)] reveals that the intensity of Pd L x-ray quanta increases only within the non-CF_x-coated line features, which reaffirm the successful self-aligned deposition of Pd via polymerized fluorocarbon growth inhibitors.

Figure 15 represents the EDX elemental mapping analyses of Pd, C, and F elements at specific patterned areas after the 2000-cycle ALD experiment. Figure 15(a) shows the SEM image of the patterned Pd line features through which elemental maps of Pd, C, and F are collected. Figures 15(b)–15(d) depict the elemental maps of C K, Pd L, and F K, respectively. It is evident from these elemental maps that Pd is present only in the line features that coincide with the Pd lines covering the non-CF_x-coated regions shown in Fig. 15(a). Overall, XPS, EDX line scan, and EDX elemental mapping cumulatively confirm the successful self-aligned patterning via selective Pd deposition using 2000-cycle ALD on lithographically patterned samples.

IV. SUMMARY AND CONCLUSIONS

In conclusion, we have presented a systematic investigation on the growth blocking/inhibition efficacy of plasma-polymerized CF_x layers to achieve selective deposition of Pt and Pd. We have demonstrated an effective yet relatively simple approach for low-temperature self-aligned patterning of Pt and Pd films using a CMOS-compatible plasma-polymerization process. The recorded nucleation delays for Pt and Pd correspond to equivalent blocking thicknesses of ~20 and ~15 nm, respectively, with selectivity values of ~0.99 for both Pt and Pd depositions. This work confirms that plasma-polymerized CF_x layers effectively inhibit film growth not only for certain oxide compounds but also for widely used noble metals (Pt and Pd). The reason for CF_x blocking layer degradation during the ozone-based ALD process was concluded to be due to the oxygen physisorption with further hydroxyl group formation on the CF_x surface that creates the favorable nucleation sites for Pt growth initiation. Our methodology can be utilized for various 3D device structures where selective Pt/Pd deposition on horizontal surfaces might be critically needed while blocking other inclined and vertical surfaces via conformally coated CF_x blocking layers. Moreover, the ozone-compatible selective deposition capability might pave the way for the AS-ALD of a wider set of materials that can benefit from ozone and alternate energetic coreactants.

ACKNOWLEDGMENTS

The authors acknowledge the Institute of Materials Science and Nanotechnology (UNAM), Bilkent University, for the growth and material characterization facilities, TUBITAK for their support under 2216 project for International Researcher, and the University of Connecticut—Research Excellence Program (REP) Grant funded by the Office of the Vice President for Research (OVPR).

DATA AVAILABILITY

The data that support the findings of this study are available from the corresponding author upon reasonable request.

REFERENCES

[1]S. F. Bent, *ASD 2017*, Eindhoven, The Netherlands, 20–21 April 2017 (2017)
[2]W.-H. Kim *et al.*, ACS Nano **10**, 4451 (2016).
[3]J. Singh, N. F. W. Thissen, N. F. W. Thissen, W. H. Kim, H. Johnson, W. M. M. Kessels, A. Bol, S. F. Bent, and A. J. M. Mackus, Chem. Mater. **30**, 663 (2018).
[4]E. Färm, M. Kemell, M. Ritala, and M. Leskelä, Thin Solid Films **517**, 972 (2008).
[5]E. Stevens, Y. Tomczak, B. T. Chan, E. A. Sanchez, G. N. Parsons, and A. Delabie, Chem. Mater. **30**, 3223 (2018).
[6]S. M. George, Chem. Rev. **110**, 111 (2010).
[7]M. Leskela and M. Ritala, Thin Solid Films **409**, 138 (2002).
[8]C. J. Serpell, J. Cookson, D. Ozkaya, and P. D. Beer, Nat. Chem. **3**, 478 (2011).
[9]A. J. M. Mackus, D. *et al.*, Chem. Mater. **25**, 1769 (2013).
[10]J. Hämäläinen, F. Munnik, M. Ritala, and M. Leskelä, Chem. Mater. **20**, 6840 (2008).
[11]M. Knez, K. Nielsch, and L. Niinisto, Adv. Mater. **19**, 3425 (2007).
[12]M. D. Groner, F. H. Fabreguette, J. W. Elam, and S. M. George, Chem. Mater. **16**, 639 (2004).
[13]B. S. Lim, A. Rahtu, and R. G. Gordon, Nat. Mater. **2**, 749 (2003).
[14]J. Tang, Q. Cao, G. Tulevski, K. A. Jenkins, L. Nela, D. B. Farmer, and S.-J. G. Han, Nat. Electron. **1**, 191 (2018).
[15]A. J. M. Mackus, A. A. Bol, and W. M. M. Kessels, Nanoscale **6**, 10941 (2014).
[16]K. Cao, J. Cai, X. Liu, and R. Chen, J. Vac. Sci. Technol. A **36**, 010801 (2018).
[17]S. Seo *et al.*, ACS Appl. Mater. Interfaces **9**, 41607 (2017).
[18]A. Mameli, M. J. M. *et al.*, ACS Nano **11**, 9303 (2017).
[19]C. R. Ellinger and S. F. Nelson, Chem. Mater. **26**, 1514 (2014).
[20]M. Junige, M. Löffler, M. Geidel, M. Albert, J. W. Bartha, E. Zschech, B. Rellinghaus, and W. F. van Dorp, Nanotechnology **28**, 395301 (2017).
[21]K. J. Park and G. N. Parsons, Appl. Phys. Lett. **89**, 043111 (2006).
[22]X. R. Jiang, H. Huang, F. B. Prinz, and S. Bent, Chem. Mater. **20**, 3897 (2008).
[23]A. J. M. Mackus, S. A. F. Dielissen, J. J. L. Mulders, and W. M. M. Kessels, Nanoscale **4**, 4477 (2012).
[24]J. Hong, D. W. Porter, R. Sreenivasan, P. C. McIntyre, and S. Bent, Langmuir **23**, 1160 (2007).
[25]M. H. Park, Y. J. Jang, H. M. Sung-Suh, and M. M. Sung, Langmuir **20**, 2257 (2004).
[26]J. R. Avila, E. J. Demarco, J. D. Emery, O. K. Farha, M. J. Pellin, J. T. Hupp, and A. B. F. Martinson, ACS Appl. Mater. Interfaces **6**, 11891 (2014).
[27]F. Sadat, M. Hashemi, B. R. Birchansky, and S. F. Bent, ACS Appl. Mater. Interfaces **8**, 33264 (2016).
[28]J.-Y. Kim, D.-S. Kil, J.-H. Kim, S.-H. Kwon, J.-H. Ahn, J.-S. Roh, and S.-K. Park, Electrochem. Soc. **159**, H560 (2012).
[29]J. Hämäläinen, M. Ritala, and M. Leskelä, Chem. Mater. **26**, 786 (2014).
[30]Z. Chen, J. Appenzeller, J. Knoch, Y. Lin, and P. Avouris, Nano Lett. **5**, 1497 (2005).

[31]A. Javey, J. Guo, Q. Wang, M. Lundstrom, and H. Dai, Nature **424**, 654 (2003).
[32]X. Luo *et al.*, Nanotechnology **26**, 164003 (2015).
[33]Y. Jiang, J. Chen, J. Zhang, A. Li, Y. Zeng, F. Zhou, G. Wanga, and R. Wang, RSC Adv. **6**, 13207 (2016).
[34]D. Gu, H. Baumgart, K. Tapily, P. Shrestha, G. Namkoong, X. Ao, and F. Müller, Nano Res. **4**, 164 (2011).
[35]K. Kim *et al.*, Nat. Commun. **5**, 4781 (2014).
[36]S. Fleischmann, A. Tolosa, M. Zeiger, B. Kruner, N. J. Peter, I. Grobelsek, A. Quade, A. Kruthd, and V. Presser, J. Mater. Chem. A **5**, 2792 (2017).
[37]K. Cao, Q. Zhu, B. Shan, and R. Chen, Sci. Rep. **5**, 8470 (2015).
[38]A. J. M. Mackus, J. J. L. Mulders, M. C. M. Sanden, and W. M. M. Kessels, J. Appl. Phys. **107**, 116102 (2010).
[39]R. H. J. Vervuurt, A. Sharma, Y. Jiao, W. M. M. Kessels, and A. Bol, Nanotechnology **27**, 405302 (2016).
[40]A. Haider, P. Deminskyi, T. M. Khan, H. Eren, and N. Biyikli, J. Phys. Chem. C **120**, 26393 (2016).
[41]A. Haider, M. Yilmaz, P. Deminskyi, H. Eren, and N. Biyikli, RSC Adv. **6**, 106109 (2016).
[42]T. Aaltonen, M. Ritala, Y.-L. Tung, Y. Chi, K. Arstila, K. Meinander, and M. Leskelä, J. Mater. Res. **19**, 3353 (2004).
[43]J. J. Senkevich, G.-R. Yang, T.-M. Lu, T. S. Cale, C. Jezewski, and W. A. Lanford, Chem. Vap. Depos. **8**, 189 (2002).
[44]J. Dendooven, R. K. Ramachandran, K. Devloo-Casier, G. Rampelberg, M. Filez, H. Poelman, G. B. Marin, E. Fonda, and C. Detavernier, J. Phys. Chem. C **117**, 20557 (2013).
[45]J. W. Elam, A. Zinovev, C. Y. Han, H. H. Wang, U. Welp, J. N. Hryn, and M. J. Pellin, Thin Solid Films **515**, 1664 (2006).
[46]M. Peukert, Electrochim. Acta **29**, 1315 (1984).
[47]T. Nakamura, S. Ichihara, and T. Den, ECS Trans. **3**, 275 (2007).
[48]M. Wakisaka, H. Suzuki, S. Mitsui, H. Uchida, and M. Watanabe, J. Phys. Chem. C **112**, 2750 (2008).
[49]T. Ioroi and K. J. Yasuda, Electrochem. Soc. **152**, A1917 (2005).
[50]B. Bhushan and Y. C. Jung, Ultramicroscopy **107**, 1033 (2007).
[51]S. Hoshian, V. Jokinen, V. Somerkivi, A. R. Lokanathan, and S. Franssila, ACS Appl. Mater. Interfaces **7**, 941 (2015).
[52]K. L. Kelly, E. Coronado, L. L. Zhao, and G. C. Schatz, J. Phys. Chem. B **107**, 668 (2003).
[53]D. Astruc, *Nanoparticles and Catalysis* (Wiley-VCH, New York, 2008).
[54]L. Xu, X.-C. Wu, and J.-J. Zhu, Nanotechnology **19**, 305603 (2008).
[55]C. Kittel, *Einfuhrung in die Festkorperphysik*, R. Oldenbourg Verlag Munchen Wien (Wiley, Frankfurt am Main, 1973), Vol. 128.
[56]See the supplementary material at https://doi.org/10.1116/6.0000701 for XPS survey scan, high-resolution XPS scans, variation in C, F at. % on CF_x/Si and C, Si at. % as a function of Pt ALD cycles, Pt binding energies on Si and CFx/Si, variation in C, F, O at. % on CFx/Si and C, Si at. % on Si as a function of Pd ALD cycles, and Pd binding energies.